Ceramics International 49 (2023) 27003–27014

Contents lists available at ScienceDirect

Ceramics International

journal homepage: www.elsevier.com/locate/ceramint

Synthesis, characterization, and supercapacitor applications of Ni-doped $CuMnFeO_4$ nano Ferrite

Pramod Agale [a], Vaibhav Salve [a], Kundan Patil [a], Satish Mardikar [b], Santosh Uke [c], Sunil Patange [d,*], Paresh More [a,**]

[a] K. E. T's, Vinayak Ganesh Vaze College Autonomous, Mulund, Mumbai, 400081, Maharashtra, India
[b] Department of Chemistry, SRS College, SGB Amravati University, Amravati, Maharashtra, India
[c] Department of Physics, JDPS College, SGB Amravati University, Amravati, Maharashtra, India
[d] Department of Physics, Shrikrishna Mahavidyalaya, Gunjoti, Maharashtra, India

ARTICLE INFO

Handling Editor: Dr P. Vincenzini

Keywords:
Sol-gel
$Cu_{1-x}Ni_xMn_{1.0}Fe_{1.0}O_4$ ferrite
Rietveld
And supercapacitor

ABSTRACT

Nickel (Ni) doped magnetically separable $Cu_{1-x}Ni_xMn_{1.0}Fe_{1.0}O_4$ ferrite was synthesized using the sol-gel auto-combustion method. The system exhibits a cubic spinel structure with a single phase in all the samples, which was confirmed using Rietveld refinement. Mixed morphology with agglomerated particles with nearly spherical/multi-faceted shapes was observed in FESEM studies. The elemental composition was confirmed from EDAX analysis. TEM images are in well accordance with FESEM images and reveals the crystalline nature of the synthesized samples. Magnetic properties of all the ferrites were studied using VSM. With the increase in the concentration Ni^{2+} the $Cu_{1-x}Ni_xMn_{1.0}Fe_{1.0}O_4$ ferrite transform from ferrimagnetic character to a superparamagnetic character. The as-synthesized materials were further tested for their electrochemical and supercapacitor applications. The electrochemical measurements revealed that $Cu_{1-x}Ni_xMn_{1.0}Fe_{1.0}O_4$ with ($x = 0.75$) exhibits superior electrochemical performance over the other samples. The high specific capacitance of 975 F g^{-1}, the high energy density of 20.8 Whkg^{-1} at a scan rate of 5 mVs^{-1}, and 94.4% capacity retention over 5000 cycles were observed for $Cu_{1-x}Ni_xMn_{1.0}Fe_{1.0}O_4$ with a concentration of $x = 0.75$.

1. Introduction

Exhaustive utilization of fossil fuels has caused very serious environmental problems to the entire world. Researchers throughout the globe are working very hard for the cleaner and more reliable energy resources to deal with environmental issues. The modern world needs a tremendous amount of energy and energy storage devices for domestic, public, and for industrial establishments. Hence energy storage devices have become very hot topic as they possess excellent storage ability as well as charge and discharge very quickly. Excellent devices for energy storage are Batteries and supercapacitors as they can store a very high amount of energy, the output power is excellent as well as they have a long life. Hence the research on supercapacitors is going with a very high speed throughout the globe [1–3]. With the extensive industrialization and modernization, the energy consumption has increased to many folds hence development of new electrode materials is in great demand to enhance the performance of energy storage systems [4,5]. Now a day's supercapacitors are considered the most promising candidates due to its simple geometry and ability to cater the energy need [6,7].

The most promising materials to be used as electrodes in the energy storage devices are the transition metal oxides. They are easily available, environment friendly, and have different constituents, morphologies, and great surface area. They exhibit higher values of specific capacitance (theoretical) [8,9]. Further, these metals play a very vital role by offering a noticeable improvement in the capacitance by tuning and controlling various defects at the surfaces as well as interfaces [10,11]. However, there are certain limitations of transition metal oxides to name a few, low electrical conductivity, sluggish ions diffusion in the bulk phase, and low electrical conductivity, these limitations lower their practical applications [12–14]. These limitations can be overcome by using spinels or ferrites. Spinels are AB_2O_4 type of compounds where, A and B are the bivalent and a trivalent metal cation respectively, if the trivalent cation is iron then they are termed ferrites [15]. The cations occupy tetrahedral (A-bivalent) and octahedral (B-trivalent) interstitial

* Corresponding author.
** Corresponding author.
E-mail addresses: smpatange@rediffmail.com (S. Patange), paresh.m34@gmail.com, pareshmore@vazecollege.net (P. More).

https://doi.org/10.1016/j.ceramint.2023.05.240
Received 28 January 2023; Received in revised form 15 May 2023; Accepted 25 May 2023
Available online 26 May 2023

positions of the FCC lattice formed by O^{2-} ions. Depending upon their crystal structure and cation distribution, the materials exhibit different electrical, magnetic, and electrochemical properties [14]. Spinel ferrites are one of the most intensively studied inorganic nanomaterials due to their versatile applications. Some of the commercial applications of ferrites are in the gas sensing [16], in the photodegradation of dyes as well as in environmental remediation [17–20], in hydrogen production [21], in the supercapacitor applications [22,23] and in the generation of energy storage devices [24]. Ferrites found tremendous application in hyperthermia [25], cytotoxicity [26] and studies on the cancer cell lines [27]. The transition metals are low-cost, environmentally friendly and their oxides are easy to synthesize. Also, the different oxidation states of transition metals are one of the boons for synthesis of different binary as well as ternary metal oxide. Out of the different transition metal oxides, the Ferrites (MFe_2O_4) are abundant in nature, environmentally friendly in nature and have different oxidation states. The ferrites (MFe_2O_4) have been widely studied for supercapacitor applications where (M = Fe, Co, Ni, Mn, Cu, Zn) [22], $NiCo_2O_4$ [28,29], $MgFe_2O_4$ [30], and $CoFe_2O_4$ [31].

Spinel ferrites consisting of a mixture of two divalent metal ions or trivalent metal cations called mixed ferrites are also reported by researchers [32,33], such ferrites are functionalized material and have tremendous applications in almost all fields. Bhujun et al. [34] synthesized $CuCoFe_2O_4$, $NiCoFe_2O_4$, and $NiCuFe_2O_4$ using sol-gel method and studied the electrochemical performance of the nanocomposite. A maximum specific capacitance of 221 Fg^{-1} was obtained with $CuCoFe_2O_4$ at a scan rate of 5 mVs^{-1}. In addition to excellent cycling stability, an energy density of 7.9 $Whkg^{-1}$ was obtained at a current density of 1 Ag^{-1}. Huang et al. [35] demonstrated that the electrical conductivity of $NiCo_2O_4$ is two or three orders of magnitude higher than the corresponding single metal oxide NiO or Co_3O_4. Chen et al. had demonstrated doping of a Ni element in Co_3O_4 and showed that there is a great enhancement in the electrical properties [36]. Thus, doping of Ni element in the ferrites increases the properties of ferrites to many folds. Due to these advantages, Ni element was selected as a dopant to synthesize $Cu_{1-x}Ni_xMn_{1.0}Fe_{1.0}O_4$ nano ferrite system with composition (x = 0.0, 0.25, 0.50, 0.75 and 1.0), using sol-gel auto-combustion method with glycine as the fuel. The as-synthesized nano ferrites were characterized using different physicochemical techniques such as XRD, FTIR, FESEM, TEM, XPS and VSM. Literature survey reveals that this is the first report in which $Cu_{1-x}Ni_xMn_{1.0}Fe_{1.0}O_4$ nano ferrites were used in the supercapacitor application.

2. Experimental

2.1. Materials

In present study, Ni $(NO_3)_2{\cdot}6H_2O$, Cu $(NO_3)_2{\cdot}6H_2O$, Mn $(NO_3)_2{\cdot}6H_2O$, and Fe $(NO_3)_3{\cdot}9H_2O$ were used as a source of nickel, copper, manganese, and iron respectively and were used to synthesize $Cu_{1-x}Ni_xMn_{1.0}Fe_{1.0}O_4$ nano ferrites. All the above salts and the reagents were purchased from Loba chemicals and were utilized to carry out synthesis of ferrite with no further purification.

2.2. Synthesis of $Cu_{1-x}Ni_xMn_{1.0}Fe_{1.0}O_4$ (X = 0.0, 0.25, 0.50, 0.75, and 1.0) nano ferrites

Sol-gel auto-combustion method was used to synthesize $Cu_{1-x}Ni_xMn_{1.0}Fe_{1.0}O_4$ nano ferrite. As per the chemical formula $Cu_{1-x}Ni_xMn_{1.0}Fe_{1.0}O_4$ (where, x = 0.0, 0.25, 0.50, 0.75, and 1.0), individual starting metal salt and the corresponding material were weighed separately. Above material was added in 20 mL of distilled water and stirred to ensure complete dissolution. This was followed by addition of 50 mL of glycine as the fuel with simultaneous dropwise addition of ammonia

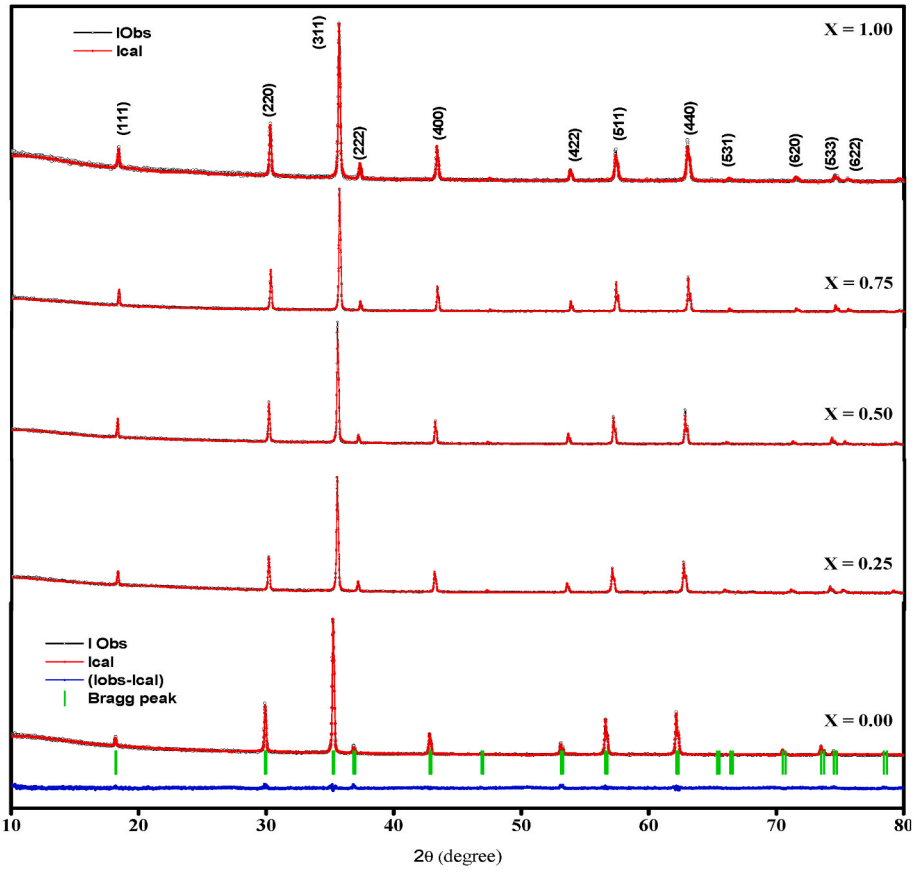

Fig. 1a. Rietveld Refined Pattern of $Cu_{1-x}Ni_xMn_{1.0}Fe_{1.0}O_4$ nano ferrite samples (x = 0.0, 0.25, 0.50, 0.75, and 1.0).

Table 1
Summary of the Rietveld refinement factors like expected factor (Rexp), weighted profile factor (Rwp), goodness-of-fit (χ^2), Crystallite size (d), lattice parameter (a), lattice parameter theoretical (ath), X-ray density (dx), r.m.s. strain and Tolerance factor (T).

Comp	Rexp	Rwp	χ2	d (nm) ±2 nm	a (Å)	ath (Å)	Dx (gm/cm3)	r.m.s. Strain (10^{-4})	Tolerance Factor T
x = 0.00	10.1	7.28	1.39	36.76	8.4200	8.4101	5.3029	0.85	1.0459
x = 0.25	7.73	5.80	1.51	50.45	8.3823	8.3929	5.3249	2.85	1.0423
x = 0.50	8.09	6.23	1.46	55.32	8.3672	8.3870	5.3489	0.76	1.0383
x = 0.75	8.83	6.79	1.36	54.79	8.3501	8.3856	5.3542	2.28	1.0410
x = 1.00	9.76	7.32	1.58	49.52	8.3450	8.3807	5.3363	1.98	1.0421

to the solution to attain a desirable pH (in the range between 8 and 9). Further, the sol so formed was converted to viscous gel by heating it at 90 °C using hot plate. The homogeneous gel was further transformed into the product by heating. The gel thus formed was ignited to cease the reaction by at once consuming all the glycine. This auto combustion process results into the formation of a brown colour residue, which was further crushed into fine powder using mortar pestle and was sintered at 800 °C in the muffle furnace for 5 h. The sintered fine powder was further characterized using various physicochemical characterization methods. Depending upon the variable Ni concentration $Cu_{1-x}Ni_xMn_{1.0}Fe_{1.0}O_4$ nano ferrite were labelled as X = 0.00, X = 0.25, X = 0.50, X = 0.75 and X = 1.00 for x = 0.00, 0.25, 0.50, 0.75, and 1.0 respectively.

2.3. Characterization

The room temperature XRD pattern of Cu1-xNixMn1.0Fe1.0O4 (X = 0.0, 0.25, 0.50, 0.75, and 1.0) nano ferrites were taken on a Philips (X pert) X-ray diffractometer using Cu kα radiation (λ = 1.5418 Å) in the 2θ range from 10 to 80°. FTIR spectra in the wavenumber range from 400 to 4000 cm− 1 were carried out using 3000 Hyperion Microscope with vertex 80 FTIR spectrometer. Morphology and the microstructure of the nano ferrites were carried out using FESEM instrument Carl Zeiss model Supra 55. TEM images were carried out on JEOL JEM 1200 EX ll instrument with an acceleration voltage of 80 kV. Magnetic measurements were carried out at room temperature using a vibrating sample magnetometer (VSM) on a Quantum Design USA make SQUID system (Model MPMS XL). XPS was carried out on a VG-ADES400 spectrometer (Al K*a* radiation).

2.4. Electrode fabrication

The substrate used for the fabrication of electrodes was stainless steel (SS) of grade 304, which functions as a current collector. The surface of the SS substrate was first cleaned in the detergent and, was dipped in 4 N HNO_3 for 30 min and finally washed using acetone followed by double distilled water and dried in the oven. Electroactive $Cu_{1-x}Ni_xMn_{1.0}Fe_{1.0}O_4$ (x = 0.0, 0.25, 0.50, 0.75, and 1.0) nano ferrite material was loaded on SS substrate as per the procedure and protocol laid down for the supercapacitor measurement [37,38]. A Homogeneous mixture of active material (85 wt %), acetylene black (5 wt %) as a conductive additive and the binder PVDF (5 wt %) were converted to a fine homogeneous mixture using mortar and pestle. This fine mixture was dispersed in dimethyl formamide (DMF) to convert it into slurry. The SS substrate was then coated with the slurry using doctor blade and dried in the oven at 60 °C and further used for the electrochemical studies. The active mass loaded on the SS plates was estimated to be in the range of 1.2–1.8 mg.

2.5. Electrochemical characterizations

Cyclic voltammetry (CV), Galvanostatic charge-discharge (GCD), and impedance spectroscopic measurements were performed using the Palmsence EmStat4s. LR electrochemical workstation forming an electrochemical cell comprising $Cu_{1-x}Ni_xMn_{1.0}Fe_{1.0}O_4$ (x = 0.0, 0.25, 0.50, 0.75, and 1.0) nano ferrites as working electrode, platinum as counter

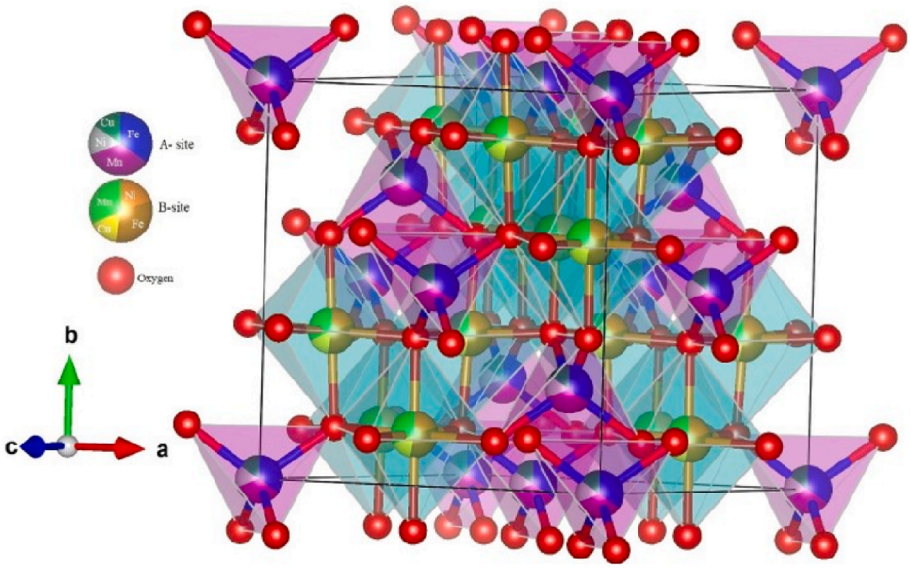

Fig. 1b. Three-dimensional Crystal structure of cubic spinel belongs to space group Fd3m of Interstitials positions partially occupied by Tetrahedral – A and Octahedral- B atom.

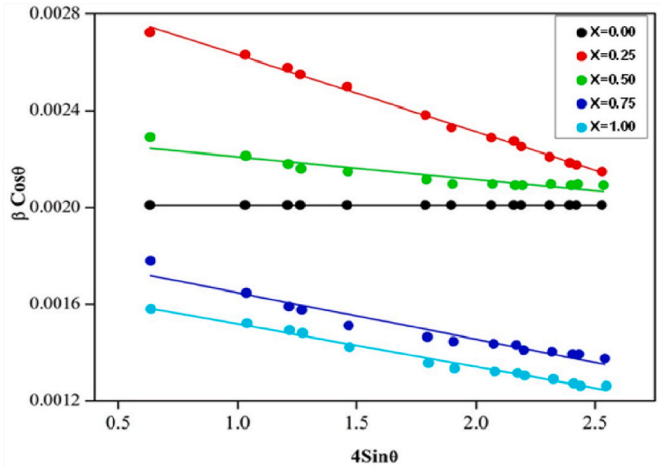

Fig. 2. Williamson hall plot of $Cu_{1-x}Ni_xMn_{1.0}Fe_{1.0}O_4$ nano ferrite samples (x = 0.0, 0.25, 0.50, 0.75, and 1.0).

electrode and Ag/AgCl as a reference electrode in 1 M Na_2SO_4 liquid electrolyte. An electrochemical impedance spectroscopic investigation of the as-synthesized material was carried out within the frequency range 1 Hz–100 kHz at open circuit potential and at 5 mV AC perturbation.

3. Result and discussion

Rietveld refined XRD pattern of $Cu_{1-x}Ni_xMn_{1.0}Fe_{1.0}O_4$ nano ferrites are depicted in Fig. 1a. Reflection at (111), (220), (311), (222), (400), (422), (511), (440), (531), (620), (533) and (622) planes correspond to the face centre cubic spinel structure. It corresponds to the structure which is a single-phase exhibiting space group Fd3m. Refinement results are tabulated in Table 1. The low values of goodness-of-fit ($\chi 2$) ranging from 1.36 to 1.58 indicates that the refinement is excellent. The low values of goodness-of-fit ($\chi 2$) range from (1.36–1.58) indicating that the refinement is excellent. A three-dimensional crystal structure of $Cu_{1-x}Ni_xMn_{1.0}Fe_{1.0}O_4$ nano ferrites obtained from the Rietveld refinement is depicted in Fig. 1b. Debye Scherrer equation as discussed elsewhere was used to calculate the crystallite size using the most intense 311 peak [39]. The results indicate that for lower doping concentrations (x = 0.0, 0.25, 0.50), the crystallite size increases from 36.76, 50.45, 55.32 and further decreases to 54.79 and 49.52 (for x = 0.75, and 1.0) respectively in the system. There is a gradual decrease in the lattice parameters (a) with the doping of Ni^{2+}ion (Table 1) this is in accordance with the Vegards law [33]. X-ray density of all the samples was calculated using the lattice parameters and depicted in Table 1. From the analysis, it is observed that, there is a slight increase in the X-ray density with the increase in concentration of nickel. Increase in the crystallinity with the

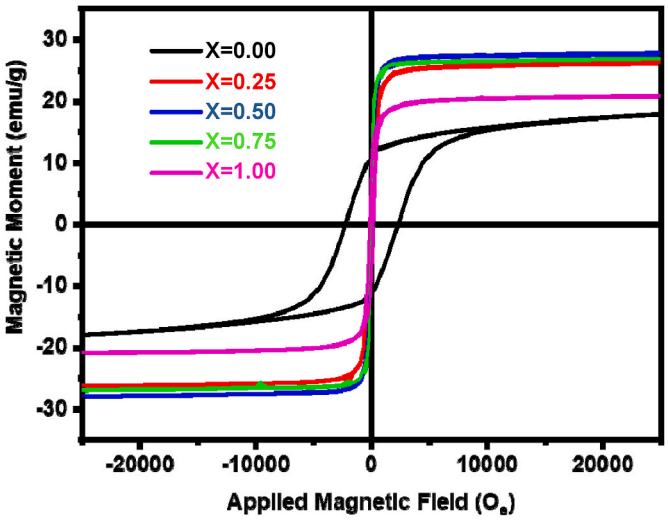

Fig. 4. Magnetic hysteresis loops for as-synthesized $Cu_{1-x}Ni_xMn_{1.0}Fe_{1.0}O_4$ nano ferrite samples (x = 0.0, 0.25, 0.50, 0.75, and 1.0).

decrease in the lattice parameters may be the factor responsible to increase in the X-ray density [33]. The r. m. s. strain of $Cu_{1-x}Ni_xMn_{1.0}Fe_{1.0}O_4$ nano ferrite were measured (Fig. 2). It is clear from Fig. 2 that the variation of sin θ with βcos θ is linear for all the samples. The straight lines obtained were extrapolated to the y axis to measure the strain. The value of the strain is listed in Table 1, very low values of the lattice strain confirm stability of structure [40].

Tolerance factor (T) was determined using following equation.

$$T = \frac{1}{\sqrt{3}}\left(\frac{r_A + R_o}{r_B + R_o}\right) + \frac{1}{\sqrt{2}}\left(\frac{R_o}{r_A + R_o}\right) \quad (1a)$$

Where rA, rB are the radii of tetrahedral and octahedral sites respectively and R_0 is the radius of the oxygen ion. The literature survey reveals that if the value of tolerance factor is close to unity, then the structure is defect free spinel's structure. The catalyst $Cu_{1-x}Ni_xMn_{1.0}Fe_{1.0}O_4$ is defect free as the value of tolerance factor is close to unity (Table 1) [40].

The FTIR spectra of $Cu_{1-x}Ni_xMn_{1.0}Fe_{1.0}O_4$ nano ferrite material were recorded from 4000 to 400 cm^{-1} range and depicted in Fig. 3a. Various positions of the bond are identified using FTIR spectra. As there is difference in the distance for oxygen ion, tetrahedral ion, and octahedral ions [40], the band positions will differ. The band at 592.58 cm^{-1} (M tet-O) are assigned for tetrahedral metal ions and oxygen ion bond whereas the band at 436.85 cm^{-1} (M oct-O) are assigned for octahedral metal ions and oxygen ion bond. In Fig. 3b with the increase in the concentration of Ni^{2+} ions the higher frequency band (M oct-O) and the lower frequency band (M tet-O) slightly shifted toward the higher and

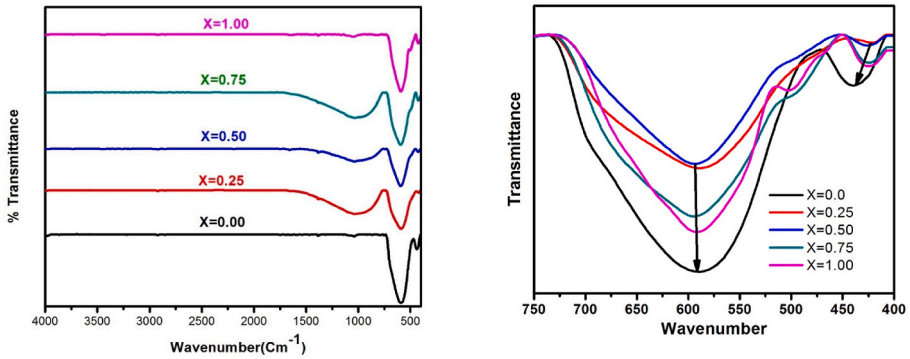

Fig. 3. FTIR sectra of as-synthesized $Cu_{1-x}Ni_xMn_{1.0}Fe_{1.0}O_4$ nano ferrite samples (x = 0.0, 0.25, 0.50, 0.75, and 1.0).

Table 2
Magnetic parameters (Saturation Magnetization Ms, Remanence Mr, Coercivity Hc, Magnetic Moment nB, Anisotropy constant K) at room temperature of $Cu_{1-x}Ni_xFeMnO_4$ system as function of Ni content (x).

Samples	Ms (emu/g)	Mr (emu/g)	Hc (Oe)	Mr/Ms	nB (μB)	K (erg/g)
x = 0.00	17.96	10.79	2287.80	0.60	0.77	42800.94
x = 0.25	26.28	0.93	27.73	0.04	1.12	759.15
x = 0.50	27.89	0.36	5.06	0.01	1.18	147.08
x = 0.75	26.98	0.76	8.47	0.03	1.14	237.90
x = 1.00	20.89	8.52	173.24	0.41	0.87	3769.94

lower wavelength respectively. These changes are observed due to the replacement of tetrahedral Cu^{2+} ion by lighter Ni^{2+} ion at the same time Ni^{2+} ions push few Fe^{3+} ions from tetrahedral site to octahedral site which replace the lighter Mn^{2+} ions [33].

The cations at the tetrahedral site (A) and octahedral site (B) are responsible for the magnetic properties of ferrites. In normal spinel ferrites the tendency of trivalent metal cation is to occupy octahedral position whereas the bivalent metal cation occupies tetrahedral position. In ferrites the net magnetization is due to the 'B' site, as 'B' site have greater magnetic moment than that of the 'A' site. The room temperature Magnetic hysteresis loops of $Cu_{1-x}Ni_xMn_{1.0}Fe_{1.0}O_4$ nano ferrites were recorded and are depicted in Fig. 4. Important parameter such as saturation magnetization (Ms), coercivity (Hc), remanent magnetization (Mr), squareness ratio (Mr/Ms), magnetic moment (nB) and anisotropy constant (K) are summarized in Table 2. An increase in the saturation magnetization was observed with the increasing concentrations of nickel. Saturation magnetization depends upon the type and the number of ions present at the tetrahedral and octahedral sites of the ferrites as the distribution of ions affects magnetization. With the increase in concentration of Ni^{2+} ions in $Cu_{1.0}$ $Mn_{1.0}$ $Fe_{1.0}O_4$ nano ferrites Ni^{2+} ions replace few Fe^{3+} ions from octahedral site to the tetrahedral site. Mn^{+3} ions spread at tetrahedral as well as octahedral site. The Ms value of $Cu_{1-x}Ni_xMn_{1.0}Fe_{1.0}O_4$ nano ferrites depends on the distribution of the magnetic Ni^{2+} (d8), Cu^{2+} (d9) and Fe^{3+} (d5) ions between the A sites (tetrahedral) and B sites (octahedral). In the present work, it was found that the Ms value (Table 2) of the nanoparticles slowly increased with the increase of the content of Ni^{2+} until x = 0.50, which is due to the magnetic Ni^{2+} ions occupying the octahedral B sites preferentially, and then slight decreased for x = 0.75 and large decrease for x = 1.00 as indicated in Table 2. Similar behaviour in Ms were reported by Jangam et al. [33]. In $Cu_{1-x}Ni_xFeMnO_4$ nano ferrite there is decrease in the remnant magnetization and coercivity up to x = 0.50 and further increase for x = 0.75 and 1.0 In $Cu_{1-x}Ni_xFeMnO_4$ nano ferrite with X = 0.0 ($Cu_{1.0}Fe_{1.0}Mn_{1.0}O_4$) the coercivity value is extremely high as compare with other concentration (X = 0.25, 0.50, 0.75 and 1.0) this is due to the distribution of Mn^{+3}, Fe^{+3} and Cu^{2+} ions over the octahedral sites [33]. Extremely high value of coercivity is further supported by the crystallite size, squareness ratio and anisotropy constant studies [15]. There is an increase in the crystallite size with the increase in the concentration of $Cu_{1-x}Ni_xFeMnO_4$ nano ferrite and found to be lowest for $Cu_{1.0}Fe_{1.0}Mn_{1.0}O_4$ (X = 0.0, Table 1). In $Cu_{1.0}Fe_{1.0}Mn_{1.0}O_4$ nano ferrite system the hysteresis loop is very broad as the material is hard magnetic material [15] and the squareness ratio Mr/Ms is highest in $Cu_{1.0}Fe_{1.0}Mn_{1.0}O_4$ for X = 0.0 system (Fig. 4 and Table 2 respectively). Further the anisotropy constant is very high for $Cu_{1.0}Fe_{1.0}Mn_{1.0}O_4$ (X = 0.0) system and decreases for the other concentration of $Cu_{1-x}Ni_x$-$FeMnO_4$ (X = 0.25,0.50,0.75) nano ferrite. Very high value of the magnetic anisotropy and low value of crystallite size are responsible for

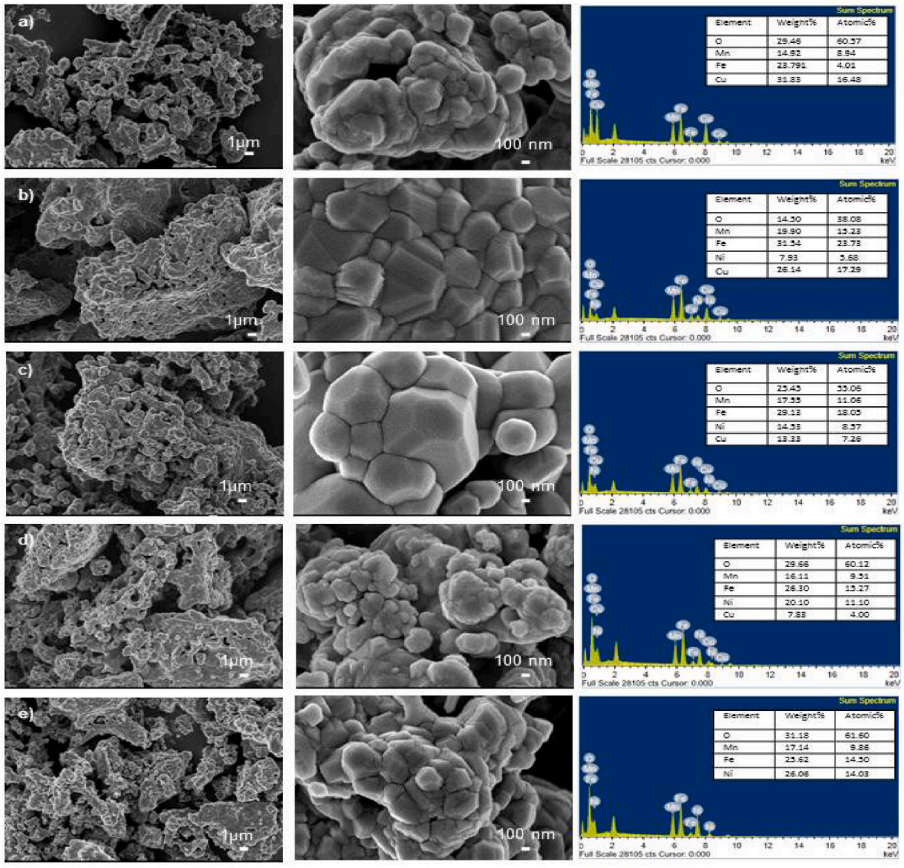

Fig. 5. Low and high resolution FESEM images of as-synthesized $Cu_{1-x}Ni_xMn_{1.0}Fe_{1.0}O_4$ nano ferrite samples (x = 0.0, 0.25, 0.50, 0.75, and 1.0) with corresponding EDS elemental mapping.

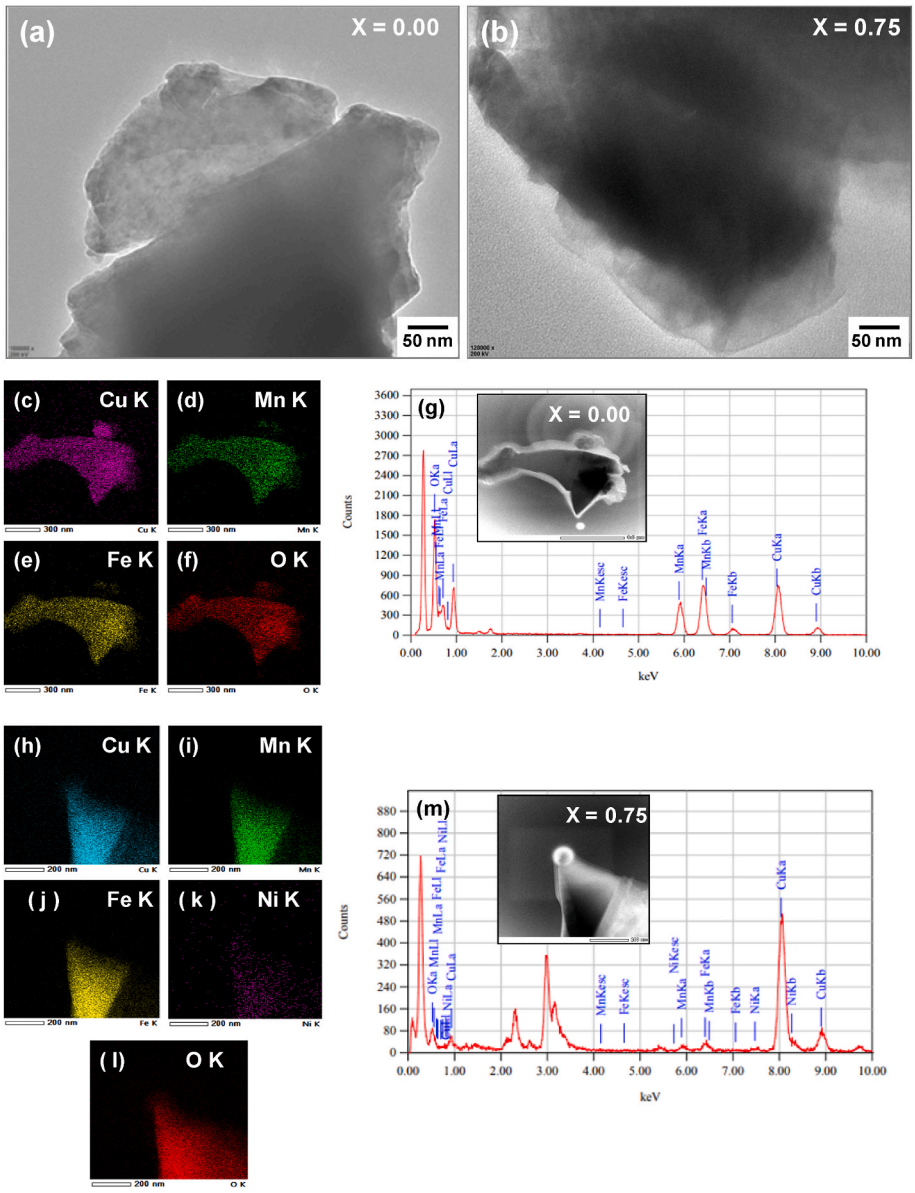

Fig. 6. (a, b) TEM images of as-synthesized representative $Cu_{1-x}Ni_xMn_{1.0}Fe_{1.0}O_4$ ferrite samples X = 0.00 and X = 0.75 respectively, (c–m) EDS elemental mapping of sample X = 0.00 and X = 0.75 respectively.

increasing coercivity of the material. Lowest particle size (Table 1), highest squareness ratio (Table 2), very high anisotropy (Table 2) is responsible for the highest coercivity in $Cu_{1.0}Fe_{1.0}Mn_{1.0}O_4$ (X = 0.0) system. Further Mn^{+3}, Fe^{+3} and Cu^{2+} ions spread over octahedral sites are responsible for the highest coercivity in $Cu_{1.0}Fe_{1.0}Mn_{1.0}O_4$ (X = 0.0) system. The squareness ratio is less than 0.10 for x = 0.25, 0.50 and 0.75 which suggest that the material is paramagnetic. Whereas for x = 0.0 and 1.0 the squareness ratio is more than 1.0 which suggest these two catalysts are ferromagnetic material [17].

The surface morphology of as-synthesized $Cu_{1-x}Ni_xMn_{1.0}Fe_{1.0}O_4$ ferrite samples were investigated with the help of FESEM. Corresponding low and high resolution FESEM images of as-synthesized $Cu_{1-x}Ni_xMn_{1.0}Fe_{1.0}O_4$ ferrite samples with changing Ni^{2+} contents x = 0.00, x = 0.25, x = 0.50, x = 0.75 and x = 1.00 (x = 0.00, x = 0.25, X = 0.50, x = 0.75 and x = 1.00) are depicted in Fig. 5. Low-resolution images of all as-synthesized samples reveal that it exhibits mixed morphology with agglomerated particles. However, a careful observation revealed from the high-resolution images indicates that most of the particles are nearly spherical/multi-faceted in shape. A pristine sample, x = 0.0 without Ni^{2+} content exhibits agglomerated morphology with irregularly shaped particles varying in size from 30 to 60 nm. The doping of Ni^{2+} in the $Cu_{1-x}Ni_xMn_{1.0}Fe_{1.0}O_4$ ferrite, results in formation of agglomerated products with well faceted crystals (sample x = 0.25 and x = 0.50). This can be attributed to the displacement of Cu^{2+} ions by lighter Ni^{2+} ions and consequently the replacement of Fe^{3+} ions from tetrahedral to octahedral sites. Further increase in Ni^{2+} contents again lead to formation of agglomerated crystal with spherical/irregularly shaped particles (sample x = 0.75 and x = 1.00). These findings are in total agreement with the XRD results. Elemental composition of $Cu_{1-x}Ni_xMn_{1.0}Fe_{1.0}O_4$ nano ferrite was confirmed using energy dispersive X-ray studies (EDS). The corresponding EDS patterns are depicted in Fig. 5. For undoped (x = 0.00) sample, peaks corresponding to the elements Cu, Mn, Fe and O are observed. For the ferrites with concentration x = 0.25, x = 0.50 and x = 0.75 the peaks of Cu, Mn, Fe, Ni, O were observed. For sample x = 1.00, there are peaks pertaining to Ni, Mn, and Fe only. Absence of any impurity peak suggest that the synthesized ferrites are pure. The microstructure of $Cu_{1-x}Ni_xMn_{1.0}Fe_{1.0}O_4$ nano ferrite was further confirmed using TEM and EDS elemental mapping. The TEM images of

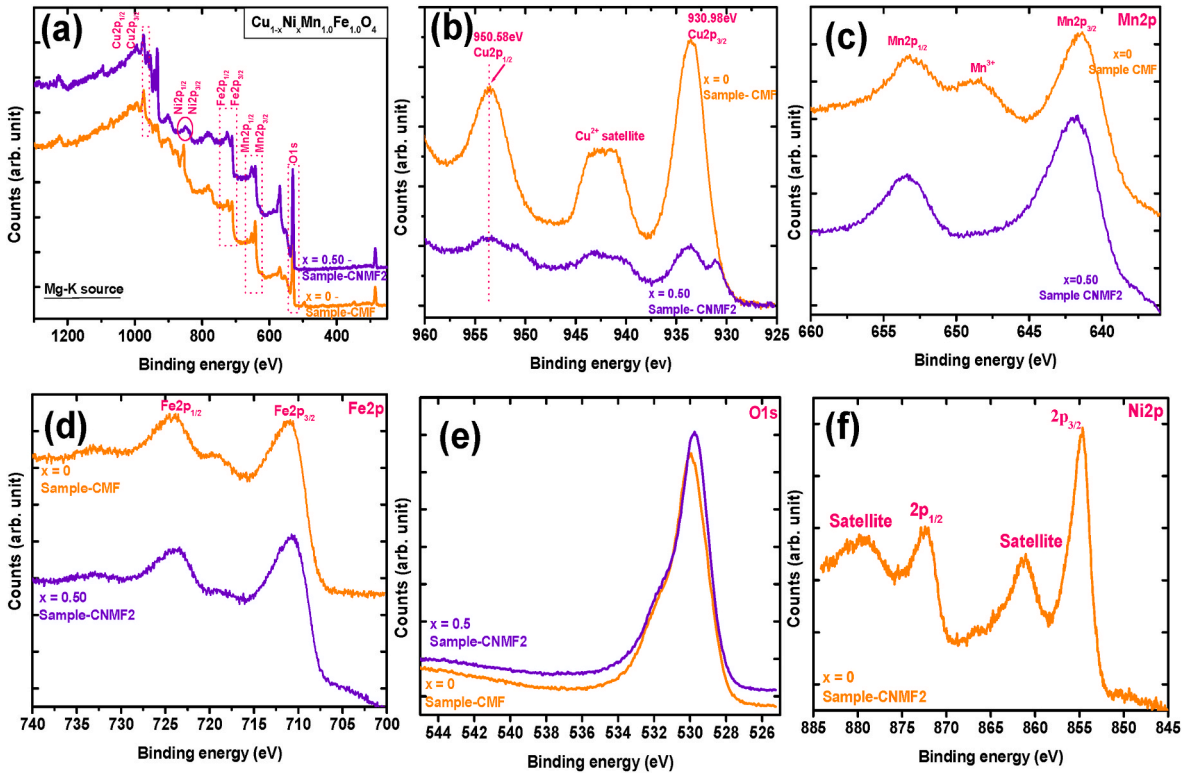

Fig. 7. XPS spectra of $Cu_{1-x}Ni_xMn_{1.0}Fe_{1.0}O_4$ ferrite:(a) survey scans for x = 0 and 0.5 (sample X = 0.00 and X = 0.50 resp.), (b)–(e) long-time measured patterns of Cu2p, Mn2p, Fe2p.

representative samples x = 0.00 and x = 0.75 are depicted in Fig. 6(a and b). The results are in well accordance with FESEM images and reveals the crystalline nature of the synthesized samples. The EDS elemental mapping of these samples is depicted in Fig. 6 (c - m) which further suggests that the nano ferrite with concentration x = 0.00 and x = 0.75 are pure and consists of Cu, Mn, Fe and Cu, Mn, Fe, Ni respectively with uniform distribution of these elements within their crystallite structure.

XPS spectroscopy was used to investigate the oxidation states as well as for the cation distribution. Survey XPS scans of the $Cu_{1-x}Ni_xMn_{1.0}Fe_{1.0}O_4$ nano ferrite with concentration of x = 0.00 and x = 0.50 respectively are depicted in Fig. 7a. In the survey scans main photo-ionization signals of metals Cu2p, Fe2p, Mn2p, oxygen O1s and Auger signals of O KLL, Fe LMM, and Ni LMM are clearly displayed.

Oxidation states, relative intensities and cationic distributions can be investigated by studying the narrow scan for long-time measured patterns of Cu2p, Mn2p, Fe2p, O1s and Ni2p bands which are depicted in Fig. 7(b–e) and (f) respectively. With concentration, x = 0.00 the peaks binding-energy positions are at 930.98 and 942.21 eV corresponds to $Cu2p_{3/2}$ and its shake-up satellite, while the weaker peak at 950.58 eV is for $Cu2p_{1/2}$ signal. Core signals of other metal ions are as follows, Mn $2p_{3/2}$ (641.7 eV) and its satellite (641.52 eV), $Mn2p_{1/2}$ (653.55 eV); Fe $2p_{3/2}$ (711.4 eV) and its satellite (719.3 eV), Fe $2p_{1/2}$ (725 eV). Further, evident XPS results confirms that the gradual increase in the Ni^{2+} content in $Cu_{1-x}Ni_xMn_{1.0}Fe_{1.0}O_4$ ferrite samples occupies on account of Cu^{2+} rather than Mn nor Fe content as can be clearly seen in of the signals intensity pattern, Fig. 7 (c) and (d). It can be clearly seen, for Mn2p and Fe2p, almost all peaks exhibit slight position shift by Ni doping with virtually same peaks intensities, Fig. 7c and (d), while gradual decrease in intensity of Cu 2P peak is observed, Fig. 7 (b). The peaks assignment indicated the most stable oxidation state of Cu^{2+}, Ni^{2+} and Fe^{2+} and dominant Mn^{2+}. Similar observation in the ferrites were reported by Patil et al. [17]. The formation of $Cu_{1-x}Ni_xMn_{1.0}Fe_{1.0}O_4$ (X = 0.0, 0.25, 0.50, 0.75, and 1.0) nano ferrite is supported by these findings.

Cyclic voltammetry (CV) technique is used to study the energy density, specific capacitance, and cycle life of the electrode material [38]. CV curves of nanocrystalline $Cu_{1-x}Ni_xMn_{1.0}Fe_{1.0}O_4$ (X = 0.0, 0.25, 0.50, 0.75, and 1.0) ferrite at different scan rate of 5–100 mVs^{-1} and voltage 0–0.8 V vs. Ag/AgCl in 1 M Na_2SO_4 electrolyte is depicted in Fig. 8(a–e). It is clear from the CV curves that with the increase in the scan rate the current under the curve gradually increases, which implies that the voltametric current is directly proportional to the scan rate. The $Cu_{1-x}Ni_xMn_{1.0}Fe_{1.0}O_4$ nano ferrite shows broad peaks. Moreover, the rectangular shape of CV curves due to the redox reaction shows the pseudocapacitive behaviour of the electrodes. Furthermore, the broad peaks as well as the rectangular shape of CV curve of as-synthesized samples originated from the redox reaction. The CV curve shows the high rate-capability is due to the high rate of intercalation and deintercalation of electrolyte ions into electrodes. This excellent high-rate performance of electrodes in electrolyte is obtained due to the mesopores structure of prepared electrode materials. The specific capacitance of the as prepared nano structured material is estimated by measuring area under the CV curve [38]. As demonstrated in Fig. 8 (a - e), the electrode $Cu_{0.25}Ni_{0.75}Mn_{1.0}Fe_{1.0}O_4$ shows better electrochemical performance than the other samples i. e. $Cu_{1-x}Ni_xMn_{1.0}Fe_{1.0}O_4$ (x = 0.0, 0.25, 0.50, and 1.0). Remarkably, the area under the CV curve for sample $Cu_{0.25}Ni_{0.75}Mn_{1.0}Fe_{1.0}O_4$ at a 5 mVs^{-1} scan rate is high as compared to other electrode samples (Fig. 8 (f)). From the CV curves, the specific capacitance (Cs) (Fg^{-1}), and energy density E ($Whkg^{-1}$) were calculated using equations (1) and (2). The $Cu_{0.25}Ni_{0.75}Mn_{1.0}Fe_{1.0}O_4$ electrode shows the high specific capacitance 975.0 Fg^{-1}, energy density 20.8$Whkg^{-1}$ at 5 mVs^{-1} and capacity retention of 94.4% over 5000 CV cycles at 100 mVs^{-1}. This excellent electrochemical activity, high specific capacitance, high cyclic stability of electrode $Cu_{0.25}Ni_{0.75}Mn_{1.0}Fe_{1.0}O_4$ is obtained due to high electrical conductivity, the perfect doping of Ni^{2+} and Mn^{2+} ions in $CuFe_2O_4$ crystals and efficient utilization pores in the 1 M Na_2SO_4 electrolyte. Moreover, the calculated specific capacitance, energy density at different scan rates, and cyclic stability over 5000 CV cycles at 100 mVs^{-1} of the $Ni_xMn_{1.0}Fe_{1.0}O_4$ (x =

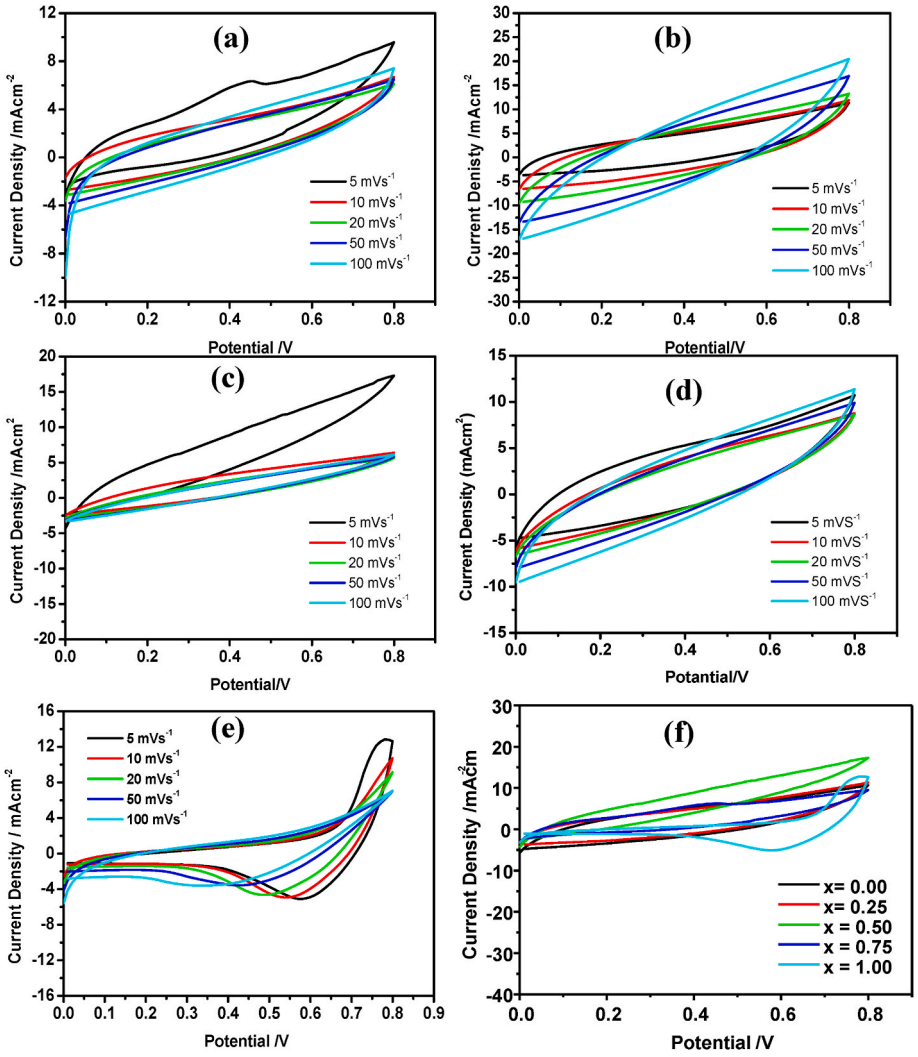

Fig. 8. Cyclic voltametric (CV) curves of nanocrystalline $Cu_{1-x}Ni_xMn_{1.0}Fe_{1.0}O_4$ sample (a) x = 0.0, (b) x = 0.25, (c) x = 0.50, (d) x = 0.75, and (e) x = 1.0 electrode samples and (f) comparison of all samples CV at 5 m Vs^{-1} scan rates in 1 mol L^{-1} Na_2SO_4 electrolyte.

Table 3
The calculated specific capacitance, energy density and cyclic stability of the $Ni_xMn_{1.0}Fe_{1.0}O_4$ (x = 0.0, 0.25, 0.50, and 1.0) samples.

Samples code	Specific capacitance (Fg^{-1})	Energy density ($Whkg^{-1}$)	Cyclic stability after 5000 cycles at 100 mVs^{-1}
x = 0.00	428.3	9.1	91.8%
x = 0.25	479.2	10.2	92.6%
x = 0.50	398.2	8.4	96.5%
x = 0.75	975.0	20.8	94.4%
x = 1.00	325.0	6.9	90.6%

0.0, 0.25, 0.50, and 1.0) samples is demonstrated in Table 3.

$$C_s = \frac{1}{mv(V_c - V_a)} \int_{V_a}^{V_c} I(V)dv \quad (1b)$$

$$E = \frac{0.5 \times C_s\left(V_{max}^2 - V_{min}^2\right)}{3.6} \quad (2)$$

Here, m is the mass deposited in (gcm^{-2}), $I(v)$ is the response current in (mA) of the sample electrode for unit area, V is the scan rate, $(V_c - V_a)$ is the operational potential window in (V), V_a anodic voltage and V_c cathodic voltage, t_d is the discharge time in (s), I_d is the discharge current (mA).

The Galvanostatic charge discharge (GCD) study of the Cu_{1-x} Ni_x Mn $_{1.0}$ $Fe_{1.0}O_4$ nano ferrite samples (x = 0.0, 0.25, 0.50, 0.75, and 1.0) was carried out at different current densities ranges from 20 $mAcm^{-2}$ to 60 $mAcm^{-2}$ within the potential window 0–0.8 V in 1 M Na_2SO_4 liquid electrolyte. Fig. 9 (a)-(e) shows the GCD curves Cu_{1-x} Ni_x Mn $_{1.0}$ $Fe_{1.0}O_4$ nano ferrite samples (x = 0.0, 0.25, 0.50, 0.75, and 1.0) of the samples at different current densities ranges from 20 $mAcm^{-2}$ to 60 $mAcm^{-2}$. Moreover, the comparative GCD curves for all Cu_{1-x} Ni_x Mn $_{1.0}$ $Fe_{1.0}O_4$ nano ferrite samples (x = 0.0, 0.25, 0.50, 0.75, and 1.0) is shown in Fig. 9 (f). Using the GCD curves, specific capacitance (Cs) (Fg^{-1}), energy density E ($Whkg^{-1}$) and power density (Wkg^{-1}) were calculated using equations (2)–(4) where, I_d is the discharge current, t_d discharge time, m is mass loaded on stainless steel electrodes and $\Delta V$is the applied potential window. The calculated specific capacitance (Fg^{-1}), energy density ($Whkg^{-1}$) and power density (Wkg^{-1}) of the Cu1.$_{-x}$ Ni_x Mn $_{1.0}$ $Fe_{1.0}O_4$ nano ferrite samples (x = 0.0, 0.25, 0.50, 0.75, and 1.0) is demonstrated in Table 4. The Cu_{1-x} Ni_x Mn $_{1.0}$ $Fe_{1.0}O_4$ nano ferrite samples with X = 0.75 show highest specific capacitance compared to other Cu_{1-x} $Ni_xMn_{1.0}Fe_{1.0}O_4$ nano ferrite samples with x = 0.0, 0.25, 0.50, and 1.0. The Cu_{1-x} $Ni_xMn_{1.0}Fe_{1.0}O_4$ nano ferrite samples with X = 0.75, show a high specific capacitance of 875 Fg^{-1}, high energy density of 19.7 $Whkg^{-1}$and a high-power density of 1.6 $kWkg^{-1}$at current density of 20 $mAcm^{-2}$. The high specific capacitance, high energy density and high-power density obtained in Cu_{1-x} $Ni_xMn_{1.0}Fe_{1.0}O_4$ nano

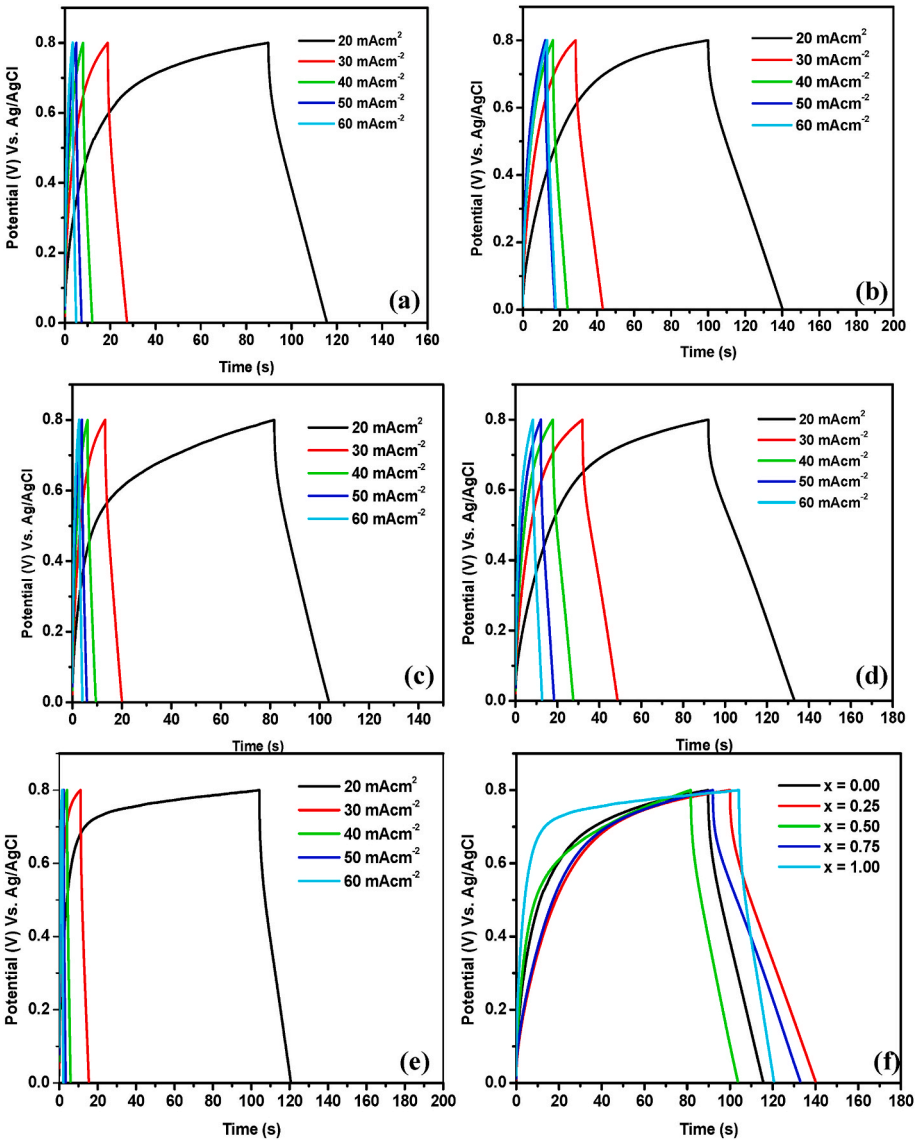

Fig. 9. GCD curves of nanocrystalline $Cu_{1-x}Ni_xMn_{1.0}Fe_{1.0}O_4$ sample (a) x = 0.0, (b) x = 0.25, (c) x = 0.50, (d) x = 0.75, (e) x = 1.0 electrode samples, and (f) the comparative GCD curve for all Cu_{1-x} Ni_x Mn $_{1.0}$ $Fe_{1.0}O_4$ nano ferrite.

Table 4
The calculated specific capacitance, energy density and power density of the $Ni_xMn_{1.0}Fe_{1.0}O_4$ (x = 0.0, 0.25, 0.50, 0.75 and 1.0) samples from GCD curves.

Samples code	Specific capacitance (Fg^{-1})	Energy density ($Whkg^{-1}$)	Power Density (Wkg^{-1})
x = 0.00	541.6667	12.0	1666.7
x = 0.25	569.4444	12.7	1111.1
x = 0.50	437.5	9.7	1666.7
x = 0.75	875	19.4	1666.7
x = 1.00	354.1667	7.8	1666.7

ferrite samples with X = 0.75. This is due to the proper doping of Ni in $CuMnFeO_4$. The proper doping of an external impurity enhances the electrical conductivity of material, and as a consequence, the electrochemical activities of the electrode at the electrode-electrolyte interface increases [39,40]. Moreover, Fig. 10 (a) and (b) demonstrate the specific capacitance obtained from CV curves at different scan rates and GCD curves at different current rates, respectively, for $Ni_xMn_{1.0}Fe_{1.0}O_4$ (x = 0.0, 0.25, 0.50, 0.75 and 1.0) samples. Interestingly, the specific capacitance obtained from the CV and GCD curves was found to be nearly equal. Fig. 10 (c) shows the plot of variation of specific capacitance verses current density curve for $Ni_xMn_{1.0}Fe_{1.0}O_4$ (x = 0.0, 0.25, 0.50, 0.75 and 1.0) samples. Fig. 10 (c) demonstrates that the specific capacitance obtained at higher current densities is remarkably lower than the specific capacitance obtained at lower current densities. This decrease in specific capacitance at higher current density is due to the inability of electrolyte ions to pour into electrode material at higher current values [41,42]. The obtained specific capacitance for the $Cu_{1-x}Ni_xMn_{1.0}Fe_{1.0}O$ for X = 0.75 is higher than the reported Mn, Fe and Ni based metal oxide electrode materials reported in recent research reports. Moreover, to illustrate the significance of this study, we have compared present study with the earlier studies reported on Mn, Fe and Ni based metal oxide electrode materials for supercapacitor applications. Moreover, to illustrate the significance of this study, we have compared the present study with the earlier studies reported in literature considering Mn, Fe, and Ni-based metal oxide electrode materials for supercapacitor applications [43–48] (Table 5).

$$C_s = \frac{I_d t_d}{(V_2 - V_1)m} \tag{3}$$

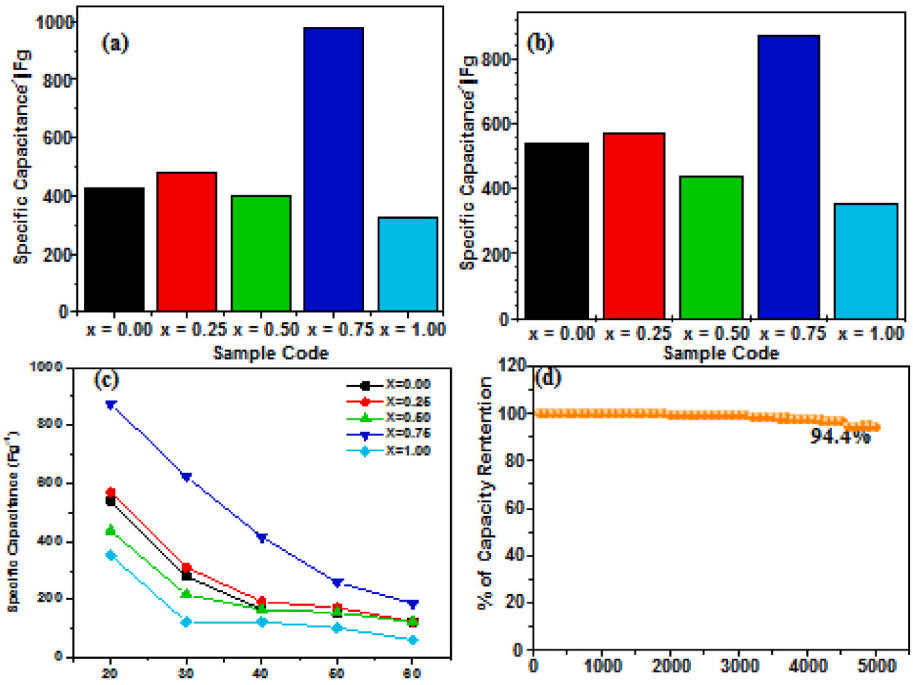

Fig. 10. Specific capacitance calculated from (a) CV curves, (b) GCD curve (c) plot of specific capacitance and current density for $Ni_xMn_{1.0}Fe_{1.0}O_4$ (x = 0.0, 0.25, 0.50, 0.75 and 1.0) samples., (d) plot of capacity retention vs. cycle number for $Ni_xMn_{1.0}Fe_{1.0}O_4$ (x = 0.75).

Table 5
Comparison of earlier studies reported for Mn, Fe and Ni based metal oxide electrode materials and present study.

Sr. No.	Material	Method of synthesis	Electrolyte	Potential window	Specific capacitance	Energy density	Power Density	% Retention of capacitance	Reference
1	$Mg_{0.1}Mn_{0.9}Fe_2O_4$	Solvothermal reflux	1 M KOH	0.0–0.6 V	226.4 Fg^{-1} at current density 0.5 Ag^{-1}	–	–	94. 6 up to 3000 cycles	[43]
2	Zn doped $MgFe_2O_4$	Sol-gel	1 M Na_2SO_4	0.0–0.4 V	484.6 Fg^{-1} at scan rate 1 $mAcm^{-2}$	10.8 $Whkg^{-1}$	0.5 $kWKg^{-1}$	–	[44]
3	$MnFe_2O_4$/graphene hybrid	Solvothermal	1.0 M H_2SO_4	0.0–0.8 V	300 F g^{-1} at a current density of 0.3 A g^{-1}	5.0 $Whkg^{-1}$	0.4 kWk^{-1}	105 after 5000 cycles	[45]
4	$MnFe_2O_4$/ graphene/PANI	Combustion	1 M NaCl	−0.55 and 0.25 V.	241 F g^{-1} at current density 0.5 mA cm^{-2},	17 $Whkg^{-1}$	–	100 after 5000 cycles	[46]
5	$NiFe_2O_4$	Chemical oxidation	2 M KOH	0–0.45 V	266 F g^{-1} at 3 mVs^{-1}	22.5 $Whkg^{-1}$	0.85 $kWkg^{-1}$	126 up to 5000 cycles	[47]
6	$MnFe_2O_4$	Combustion	0.1 M HCl and 0.1 M $NaNO_3$	−1.0–1.2 V and −1.6 to 1.6 V for 0.1 M HCl and 0.1 M $NaNO_3$ electrolyte, respectively	297.7 Fg^{-1} current density 1 Ag^{-1} (in 1 M HCl)	–	–	92 for 0.1 M HCl for and 90 for 0.1 M $NaNO_3$ after 2500 cycles	[48]
7	$MnFe_2O_4$/GO	Co-precipitation	6 M KOH	−0.9-0.2 V	298 F g^{-1} at current density of 1 A/g	–	–	92 up to 500 cycles.	[49]
8	$MnFe_2O_4$	Chemical oxidation	2 M KOH	0.0–0.45 V	415 Fg^{-1} current density 1 Ag^{-1}	–	–	104 up to 3000 cycles	[50]
9	carbon modified Fe_3O_4	chemical oxidation	6 M KOH	−0.8-0.3 V	274 F g^{-1} at current density 0.5 Ag^{-1}	–	–	83 up to 5000 cycles	[51]
10	$Cu_{1-x}Ni_xMn_{1.0}Fe_{1.0}O$ for X = 0.75	Auto-combustion	1 M Na2SO4	0.0–0.8 V	875 Fg^{-1}, at current density of 20 $mAcm^{-2}$.	20.8 Wh kg^{-1}	1.7 4 $kWkg^{-1}$	94.4 after 5000 cycles	Present work

$$P = \frac{E \times 3600}{t_d} \quad (4)$$

Electrolyte resistance (R_s) as well as the charge–transfer resistance (R_{ct}) of $Cu_{1-x}Ni_xMn_{1.0}Fe_{1.0}O_4$ (x = 0.0, 0.25, 0.50, 0.75, and 1.0) nano ferrite was calculated using electrochemical impedance spectroscopy (EIS). The EIS study of the samples was carried out at an open circuit potential of 5 mV a. c. within the frequency range from 1 Hz to 100 kHz. The Nyquist plot of $Cu_{1-x}Ni_xMn_{1.0}Fe_{1.0}O_4$ (x = 0.0, 0.25, 0.50, 0.75, and 1.0) nano ferrite sample electrodes are depicted in Fig. 11. The electrolyte resistance (R_s) is also called equivalent series resistance. The electrolyte resistance (R_s) is obtained from the high–frequency intercept of the semicircle on the real axis of the Nyquist plot. Moreover, the diameter of the semicircle of high–frequency intercept on the real axis of the Nyquist plot gives the charge-transfer resistance (R_{ct}) [38]. The

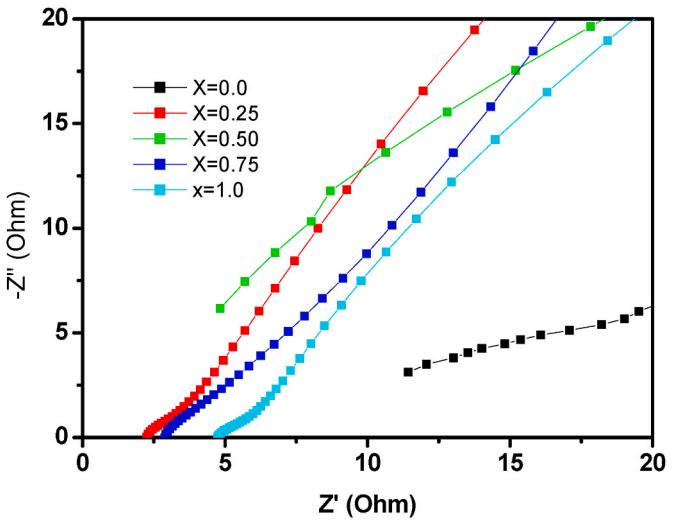

Fig. 11. The complex impedance plot (Nyquist plot) of nanocrystalline $Cu_{1-x}Ni_xMn_{1.0}Fe_{1.0}O_4$ (x = 0.0, 0.25, 0.50, 0.75, and 1.0) samples.

Table 6
Electrolyte and charge transfer resistance of the $Ni_xMn_{1.0}Fe_{1.0}O_4$ (x = 0.0, 0.25, 0.50, 0.75 and 1.0) samples.

$Cu_{1-x}Ni_xMn_{1.0}Fe_{1.0}O_4$ electrodes for different x	Electrolyte resistance (R_s) (Ω)	Charge–transfer resistance (R_{ct}) (Ω)
x = 0.00	9.8	8.2
x = 0.25	2.4	2.66
x = 0.50	2.5	1.98
x = 0.75	1.5	1.8
x = 1.00	4.9	3.9

electrolyte resistance (R_s)/equivalent series resistance consists of electronic and ionic contribution. Whereas interfacial resistance corresponds to inter–particles resistance and resistance between particles and current collector. Low values of electrolyte resistance (R_s), and charge transfer resistance (R_{ct}) is responsible for easy access for intercalation and de–intercalation of ions on the electrode surface, and facile charge-transfer at electrode-electrolyte interface. From Nyquist plot the electrolyte resistance (R_s) as well as charge–transfer resistance (R_{ct}) of $Cu_{1-x}Ni_xMn_{1.0}Fe_{1.0}O_4$ (x = 0.0, 0.25, 0.50, 0.75, and 1.0) nano ferrite is calculated as demonstrated in Table 6. From Table 6, the sample $Cu_{1-x}Ni_xMn_{1.0}Fe_{1.0}O_4$ with x = 0.75 resulted in the low values of electrolyte resistance (R_s) 1.5 Ω and charge–transfer resistance (R_{ct}) 1.8 Ω. Interestingly, the results obtained from EIS are in good agreement with the results obtained from CV and GCD studies. Hence, the electrode materials synthesized in this study exhibit excellent electrochemical performance and could serve as potential candidates for electrode fabrication, with the potential for use in high-energy density supercapacitor applications.

4. Conclusion

In summary, Ni-doped $Cu_{1-x}Ni_xMn_{1.0}Fe_{1.0}O_4$ nano ferrites having five different compositions (x = 0.0, 0.25, 0.50, 0.75 and 1.0) were synthesized by sol-gel auto-combustion method and were characterized with the help of various physicochemical techniques such as XRD, FTIR, SEM, TEM, XPS and VSM. The outstanding electrochemical performance demonstrated by the as-prepared nanostructure $Cu_{1-x}Ni_xMn_{1.0}Fe_{1.0}O_4$ with X = 0.75 can be attributed to the uniform morphology, appropriate doping at active sites, and high electrical conductivity. These factors have led to the high specific capacitance (975 Fg^{-1}), high energy density (20.8 $Whkg^{-1}$) at a scan rate of 5 mVs^{-1}, and remarkable capacity retention (94.4%) over 5000 cycles. The exceptional electrochemical performance of the as-synthesized samples highlights their high practicability as potential electrode materials in the fabrication of high energy density supercapacitors. With their stability and durability, these materials could significantly contribute to the development of advanced energy storage technologies and hold promise for a sustainable energy future.

Credit author statement

Contribution of Authors in the manuscript: Credit author statements are as follows. Mr. Pramod Agale: Format analysis, Methodology, Investigation, Supercapacitor studies, Mr. Vaibhav Salve: Plotting of the graphs, Synthesis of Material, Mr. Kundan Patil: Synthesis of ferrites, Plotting of graphs, Dr. Satish Mardikar: Synthesis of ferrites, Plotting of graphs, Dr. Santosh Uke: Electrode preparation, Software, Project Administration, Dr. Sunil Patange: Plotting, software run of Rietveld, Dr. Paresh More: Conceptualization of idea, writing review and editing, writing original manuscript and supervision.

Declaration of competing interest

There are no conflicts to declare.

Acknowledgements

PMA, VMS and PSM are thankful to the Management and Principal Prof. Preeta Nilesh of K. E. T'S, V. G. Vaze College Autonomous for encouragement and support.

References

[1] J. Chen, J. Xu, S. Zhou, N. Zhao, C.P. Wong, Nano Energy 21 (2016) 145–153.
[2] S. Mardikar, S. Balgude, S. Uke, Intech Open (2021), https://doi.org/10.5772/intecopen.98355.
[3] S. Uke, S. Mardikar, Nanowires for metal-ion Batteries, in: Nanowires, CRC Press, eBook ISBN9781003296621, 2023, pp. 65–81.
[4] S. Uke, S. Mardikar, A. Kumar, Y. Kumar, M. Gupta, Y. Kumar, Royal Society open science, 2021, https://doi.org/10.1098/rsos.210567.
[5] W.H. Qu, F. Han, A.-H. Lu, C. Xing, M. Qiao, W.C. Li, J. Mater. Chem. 2 (2014) 6549–6557.
[6] C. Liu, F. Li, L.P. Ma, H.M. Cheng, Adv. Mater. 22 (2010) 28–62.
[7] Y. Dai, S. He, L. Yu, J. Liu, L. Gan, M. Long, J. Phys. Chem. Solid. 129 (2019) 122–127.
[8] A. Thirumurugan, T. Kavinkumar, R. Udayabhaskar, R. Kiruthiga, M. Morel, R. Aepuru, N. Dineshbabu, K. Ravichandran, A. Akbari-Fakhrabadi, R. Mangalaraja, Electrochim. Acta 399 (2021) 10, 139346.
[9] S. Uke, et al., A Review of π-conjugated Polymer-Based Nanocomposites for Metal-Ion Batteries and Supercapacitors, vol. 10, Royal Society Open Science8, 2021, 210567.
[10] Z. Yu, L. Tetard, L. Zhai, J. Thomas, Energy Environ. Sci. 8 (2015) 702–730.
[11] X. Lu, C. Wang, F. Favier, N. Pinna, Adv. Energy Mater. 7 (2017), 1601301.
[12] Y. Xu, X. Wang, C. An, Y. Wang, L. Jiao, H. Yuan, J. Mater. Chem. 2 (2014) 16480–16488.
[13] S. Raj, P. Kar, P. Roy, Chem. Commun. 54 (2018) 12400–12403.
[14] K. Yogesh, et al., J. Nanoparticle Res. 5 (2021) 119.
[15] K. Patil, S. Kadam, P. Lokhande, S. Balgude, P. More, Solid State Commun. 337 (2021), 114435.
[16] A. Sutka, A. Gross, Sensor. Actuator. B Chem. 222 (2016) 95–105.
[17] K. Patil, K. Jangam, S. Patange, S. Balgude, A.G. Al-Sehemi, H. Pawar, P. More, J. Phys. Chem. Solid. 167 (2022), 110783.
[18] K. Jangam, A. Nair, K. Patil, S. Balgude, A. Kulkarni, P. More, Micro and Nano Technologies (2021) 329–347.
[19] S. Balgude, K. Patil, S. Moharil, M. Puranik, S. Kadam, P. Lokhande, S. Patange and P. More, ChemistrySelect, doi.org/10.1002/slct.202200221.
[20] K. Jangam, S. Balgude, H. Pawar, S. Patange, P. More, Surface. Interfac. 33 (2022), 102189.
[21] J. Domínguez-Arvizu, J. Jimenez-Miramontes, J. Salinas-Gutierrez, M. Melendez-Zaragoza, A. Lopez-Ortiz, V. Collins-Martínez, Int. J. Hydrogen Energy 44 (2019) 12455–12462.
[22] M. Aparna, A. Grace, P. Sathyanarayanan, N. Sahu, J. Alloys Compd. 745 (2018) 385–395.
[23] A. Manohar, V. Vijayakanth, S. Prabhakar Vattikuti, Ki Hyeon Kim, Mater. Chem. Phys. 301 (2023), 127601.
[24] M. Ala, V. Vijayakanth, S. Prabhakar Vattikuti, Ki Hyeon Kim, Ceram. Int. 49 (12) (2023) 19717–19727.
[25] M. Ala, V. Vijayakanth, P. Manivasagan, E. Jang, B. Hari, M. Gu, Ki Hyeon Kim, Mater. Chem. Physics287 (2022), 126295.

[26] M. Ala, V. Vijayakanth, S. Prabhakar Vattikuti, Ki Hyeon Kim, Mater. Chem. Phys. (2022), 126117.
[27] M. Ala, V. Vijayakanth, S. Prabhakar Vattikuti, P. Manivasagan, E. Jang, K. Chintagumpala, Ki Hyeon Kim, ACS Appl. Nano Mater. 5 (4) (2022) 5847–5856.
[28] S. Uke, V. Akhare, S. Mardikar, A. Bodade, Gajanan N. Chaudhari, Adv. Sci. Eng. Med. 5 (2019) 357–366.
[29] S. Uke, G. Chaudhari, A. Bodade, S. Mardikar, Materials Science for Energy Technologies 3 (2020) 289–298.
[30] S. Uke, S. Mardikar, D. Bambole, Y. Kumar, G. Chaudhari, Materials Science for Energy Technologies3 (2020) 446–455.
[31] H. Gao, J. Xiang, Y. Cao, Appl. Surf. Sci. 413 (2017) 351–359.
[32] K. Jangam, K. Patil, S. Balgude, S. Patange, P. More, RSC Adv. 10 (2020), 42766.
[33] K. Jangam, K. Patil, S. Balgude, S. Patange, P. More, J. Phys. Chem. Solid. 148 (2021), 109700.
[34] B. Bhujun, M. Tan, A. Shanmugam, Results Phys. 7 (2017) 345–353.
[35] L. Huang, D. Chen, Y. Ding, S. Feng, Z. Wang, M. Liu, Nano Lett. 13 (2013) 3135–3139.
[36] S. Chen, M. Xue, Y. Pan, L. Zhu, S. Qiu, J. Mater. Chem. 3 (2015) 20145–20152.
[37] P. Vardhan, C. Vishnu, U. Jothilakshmi, M. Kamachi, S. Devaraj, Mater. Today Proc. 13 (2017) 12407–12415.
[38] S. Uke, G. Chaudhari, Y. Kumar, S. Mardikar, Mater. Today Proc. (2021) 2792–2799.
[39] Y. Yang, H. Chen, R. Nie, C. Li, S. Xu, M. ZhouM, H. Zhou, J. Alloys Compd. 935 (2023), 167958.
[40] C. Yan, E. Han, X. Yang, K. Hu, H. Xu, Y. Li, S. Lu, Ceramics International, 2023, https://doi.org/10.1016/j.ceramint.2023.01.002.
[41] A. Pal, S. Ghosh, D. Singha, M. Nandi, ACS Appl. Energy Mater. 4 (10) (2021) 10810–10825.
[42] S. Li, J.G. Zhang, Y.Y. Yan, L.L. Yu, J.T. Zhao, J. Energy Storage 59 (2023), 106456.
[43] A. Manohar, V. Vijayakanth, S. Vattikuti, K.H. Kim, Ceram. Int. 48 (20) (2022) 30695–33070.
[44] S. Uke, S. Mardikar, D. Bambole, Y. Kumar, G. Chaudhari, Materials Science for Energy Technologies 3 (2020) 446 455.
[45] W. Cai, T. Lai, W. Dai, J. Ye, J. Power Sources 255 (2014) 170–178.
[46] S. Vijaya, R. Selvan, Journal of Power Sources275 (2015) 399–407.
[47] S. Meena, K. Anantharaju, S. Malini, A. Dey, L. Renuka, S. Prashantha, Y. Vidya, Ceram. Int. 10 (2021) 14723–14740.
[48] S. Meena, K. Anantharaju, S. Malini, A. Dey, L. Renuka, S. Prashantha, Y. Vidya, Ceram. Int. 47 (10) (2021) 14723–14740.
[49] N. Foroutan, M. Lashkenari, E. Alizadeh, M. Sedighi, International Journal of Hydrogen Energy, 2023, https://doi.org/10.1016/j.ijhydene.2023.03.148.
[50] A. Thirumurugan, T. Kavin Kumar, T.R. Udayabhaskar, M. Morel, G. Rajesh, R. Mangalaraja, A. Akbari-Fakhrabadi, Mater. Lett. 276 (2020), 128240.
[51] A. Thirumurugan, K. Prabakaran, R. Udayabhaskar, R. Mangalaraja, A. Akbari-Fakhrabadi, Appl. Surf. Sci. 485 (2019) 147–157.